Acta Materialia 231 (2022) 117842

Contents lists available at ScienceDirect

Acta Materialia

journal homepage: www.elsevier.com/locate/actamat

Overview article

3D *in situ* study of damage during a 'shear to tension' load path change in an aluminium alloy

Xiang Kong[a], Lukas Helfen[b,d], Mathias Hurst[b,c], Daniel Hänschke[b], Djamel Missoum-Benziane[a], Jacques Besson[a], Tilo Baumbach[c], Thilo F. Morgeneyer[a,*]

[a] MINES ParisTech, PSL University, Centre des Matériaux, CNRS UMR 7633, Evry, France
[b] Institute for Photon Science and Synchrotron Radiation (IPS), Karlsruhe Institute of Technology (KIT), 76344 Eggenstein-Leopoldshafen, Germany
[c] Laboratory for Applications of Synchrotron Radiation (LAS), Karlsruhe Institute of Technology (KIT), 76131 Karlsruhe, Germany
[d] Institut Laue–Langevin, CS 20156, 38042 Grenoble Cedex 9, France

ARTICLE INFO

Article history:
Received 28 January 2022
Revised 11 March 2022
Accepted 11 March 2022
Available online 16 March 2022

Keywords:
Ductile damage
Aluminium alloy
Tomography
Laminography
Digital volume correlation

ABSTRACT

A load path change (LPC) from shear to tension has been studied for a recrystallized 2198 T8 aluminium alloy sheet material by three-dimensional (3D) X-ray imaging combined with image correlation and interpreted by complementary 3D finite element (FE) simulations. A cross-shaped specimen was designed for the non-proportional loading and multiscale study. The effect of the LPC on the formability and related strain localisation, damage and failure was investigated and damage mechanisms could be clearly identified. The macroscopic tension stretch to fracture, measured by an optical extensometer during the shear to tension test, was reduced by about 20% compared to the proportional tension test. Damage, measured by *in situ* laminography imaging at μm-scale resolution, has interestingly already been found under shear, and was quantified as surface void fraction during the LPC. Strain was measured inside the material and at the mesoscale by 2D digital image correlation (DIC) on projected volume data, using the (natural) intermetallic particle contrast present in the 3D laminographic data. An accumulated equivalent strain definition, suited for the description of non-proportional loading, has been applied to the DIC data and FE simulations, indicating good agreement between both. On the microscopic scale, damage was seen to nucleate under shear load in the form of flat cracks, of similar width as the grain size, and in the form of cracks inside intermetallic particles. This damage subsequently grew and coalesced during tensile loading which in turn led to final fracture.

1. Introduction

Whilst research has focused for decades on damage and fracture at high levels of triaxial stress during proportional loading of thick components containing severe notches [1], only more recently [2] deformation and failure at lower levels of stress triaxiality, i.e. below 1, have been considered. In high stress triaxiality fracture the nucleation, growth and coalescence of voids are the main damage mechanisms and stress triaxility in combination with plastic strain are identified as the driving forces of ductile damage growth [1].

However, at low levels of stress triaxiality, complex non-monotonic relationships between strain at fracture and stress triaxiality have been found [2]. The definition and measurement of fracture strains in these circumstances are difficult due to the highly localised final failure process [3]. Rather phenomenological models considering strain, stress triaxiality and the Lode parameter have been used to try to fit the experimental behaviour [2]. Void growth is very limited under shear as the stress triaxiality is close to zero.

Most engineering structures undergo load path changes during forming and/or during forming followed by in-service loading. At the macroscopic level even more complex and unexplained relationships between fracture strain for load path changes (LPC) were found [4]. Brünig et al. [4] used H-shaped specimens to investigate a 'shear to tension' load path change for a 6082 T6 aluminium alloy. A reduction in macroscopic displacement was found when a shear pre-strain was applied before applying the tensile strain. The higher the pre-strain the higher the reduction in tensile strain. There is a lack of knowledge about the damage mechanisms

* Corresponding author.
E-mail address: thilo.morgeneyer@mines-paristech.fr (T.F. Morgeneyer).

https://doi.org/10.1016/j.actamat.2022.117842

under these conditions. In consequence, fracture due to load path changes is hard to predict even though it is highly application relevant.

Even the ductile damage mechanisms under monotonic low stress triaxiality loading are less clear than under high stress triaxiality loading. Gross and Ravi-Chandar [5] investigated deformation and failure of Al 6061-T6 under shear loading via *in situ* SEM. They found that second phase particles broke, debonded or rotated. Incipient voids had a minimal influence on the deformation of this material under shear. Achouri et al. [6] found for an HSLA steel that voids nucleated on the particle-steel interface, rotated and elongated with increasing shear strain. These surface observations are subject to surface preparation artefacts and free surface effects such as the onset of surface roughness during straining.

With recent advances in synchrotron three-dimensional (3D) imaging, damage inside the material bulk can to be studied both qualitatively and quantitatively *in situ* [7,8]. Synchrotron laminography is suited to image regions of interest in large flat samples at micrometer resolution [9], thereby guaranteeing that relevant mechanical conditions are present in the bulk of the material compared to surface observations. Basic failure mechanism at low triaxiality (i.e. shear) have been explored [10,11] via this non-destructive 3D imaging technique. Roth et al. [10] observed void nucleation and growth on rigid hard particles in ferrite-bainite steel under shear-dominant loading via laminography and validated shear damage phase via a 2D RVE analysis. Voids nucleated due to particle-matrix de-cohesion, subsequently elongated and aligned with the principal strain direction. Tancogne-Dejean et al. [11] observed and followed statistically intermetallic particles and pre-existing voids under low stress triaxiality proportional shear loading for a ductile Al alloy AA2024-T3. It was found that intermetallic particles broke with cracks normal to the principal stress direction. Pre-existing voids were shown to rotate and close.

Using the 3D *in situ* images, strain inside the material can be computed via tracking if the natural image contrast, caused by the material microstructure, e.g. intermetallic particles, is sufficient. This digital volume correlation has been successfully applied to aluminium alloys [12–14]. 2D image correlation of projected 3D data may be an alternative method when the contrast in the 3D image is low [10,11,14,15].

Concerning the micromechanical modelling of damage mechanisms under shear loading, Fleck et al. [16] investigated the effect of void nucleation from rigid particles and growth on macroscopic stress-strain behaviour under shear and their softening effect in a shear band. They found that accounting for particle matrix contact was important. Tvergaard [17,18] simulated 2D void behaviour under simple shear and found void rotation and elongation. This process leads to final closure of voids and also to macroscopic localization. A 3D simulation for spherical voids have been carried out in [19]. Torki and Benzerga [20] investigated the process of void-mediated failure inside a naturally forming, i.e. stress triaxiality larger than zero, shear band and carried out numerical simulations using a continuum micromechanics framework for dilatant plasticity that captured the essential features of sub-cell deformation: a. void-induced strain localization; b. void rotation; c. void elongation. In Nahshon et al. [21], a modification of the Gurson model was proposed to account for softening under shear supposing the presence of initial porosity. Most of these theoretical works still need experimental validation.

The material employed here is one of the third generation Al-Cu-Li alloys with higher copper over lithium ratio compared to the second generation [14,22]. More precisely, the fuselage sheet alloy AA2198 in T851 temper (*i.e.* solutionized, stretched and artificially aged) is used in its recrystallized state [23,24]. The alloy has an optimized and attractive balance of tensile strength (500 MPa in rolling direction) and toughness amongst this class of third generation alloys (*e.g.* 2098T8) [22], and shows good properties after friction stir welding [25]. Its failure mechanisms were identified as intergranular and transgranular in [13,26]. Sub micrometre dimples were found in the slant fracture zones.

The aim of this work is to study the effect of a load path change from 'shear to tension' at low stress triaxiality on ductility, on deformation and on damage mechanisms. The experimental approach, including material, sample design and *in situ* X-ray laminography testing is introduced first. At the mesoscale, an accumulated equivalent strain is defined for load path changes and applied to both experimental digital image correlation (DIC) and numerical finite element (FE) calculations. The interaction between strain and damage evolution is assessed via DIC performed on projected 3D X-ray laminography data and the corresponding micro damage features are tracked and quantitatively analysed in terms of surface void fraction during loading. At the microscopic scale, the damage mechanisms related to the material microstructure are then analysed. The spatial distributions of the equivalent strain and stress triaxiality are extensively analysed for the loading steps by FE simulation using an anisotropic plasticity model.

2. Experimental procedure

2.1. Material

The material of interest in this study was a 2198 T851 alloy in recrystallized form, referred to as 2198T8R henceforth. Its nominal composition is given in Table 1.

Moderate plastic anisotropy was found in different loading directions: the rolling direction is noted as L, the long transverse direction as T, short transverse direction (thickness direction) as S and the diagonal direction (45° between L and T in the sheet plane) as D.

Electron Back-Scatter Diffraction (EBSD) analysis was performed in an FEI Nova nanosem 450FEG with an EDAX-TSL Hikari EBSD camera using a step size of 0.5 μm and an acceleration voltage of 15 kV. Large recrystallized pancake-shaped grain structure was obtained in the LT plane shown in Fig. 1 (a). The grain size was measured by a mean linear intercept method as 82 μm in L, 80 μm in T and 20 μm in S directions. The material can be considered as homogeneous along the S direction without any grain size gradient [27]. 2D sections of undeformed material 2198T8R from synchrotron radiation computed laminography (SRCL) [9] image data are shown in Fig. 1 (b). The intermetallic particle (white) volume fraction is ∼0.3-0.4% while initial porosity (black) is negligible down to less than 0.03 vol.% in the aluminium matrix (grey). Moderate texture via EBSD is presented in pole figure (c).

2.2. Mechanical testing

2.2.1. Specimen geometries

Inspired by the geometry given in Roth et al. [28] and in order to perform the load path change tests, new specimen geometries,

Table 1
Chemical composition limits of 2198 alloy in weight percent(wt.%) [27].

	Cu	Li	Zn	Mn	Mg	Zr	Si	Ag	Fe
wt.%	2.9-3.5	0.8-1.1	≤ 3.5	≤ 0.5	0.25-0.8	0.04-0.18	≤ 0.08	0.1-0.5	≤ 0.01

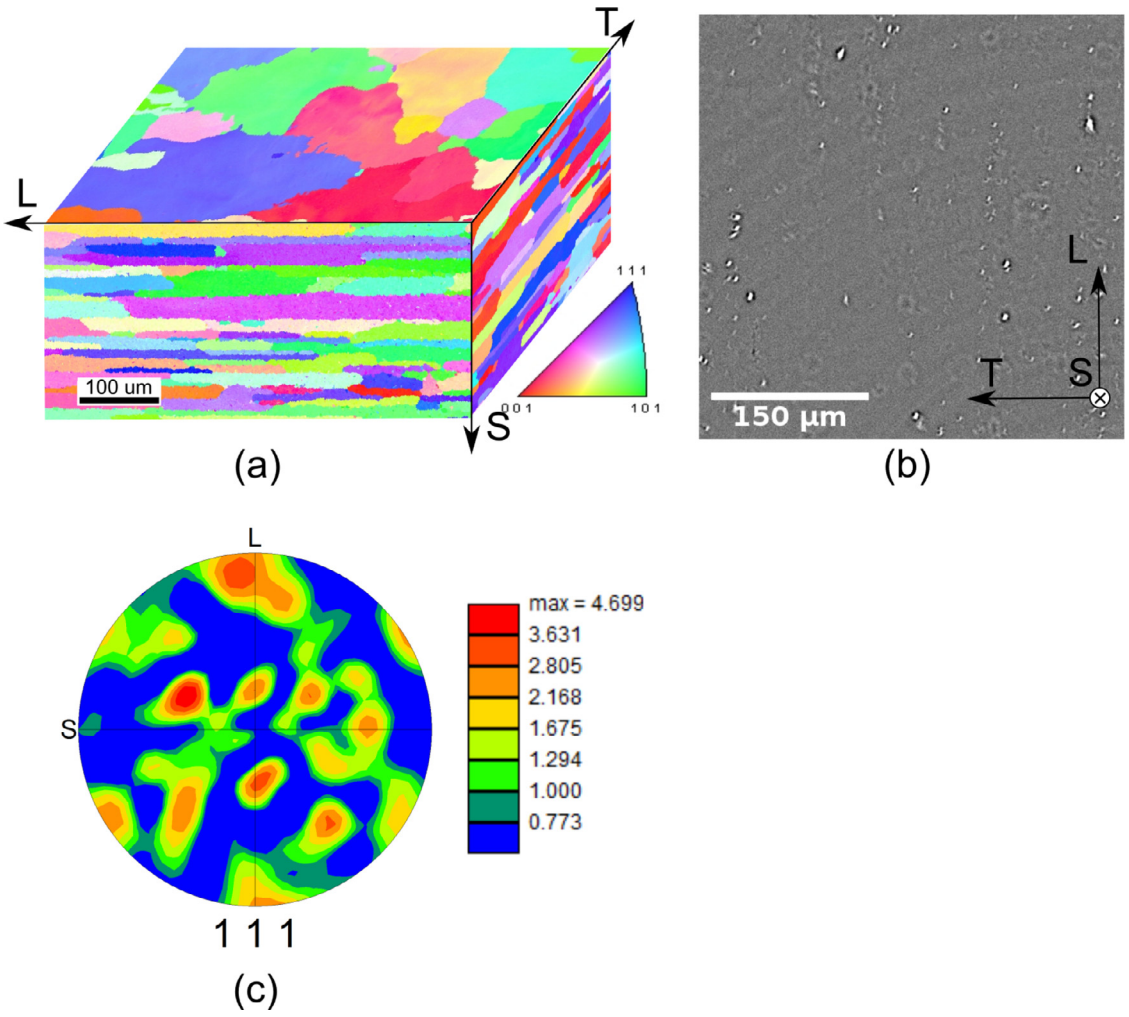

Fig. 1. (a) Inverse pole figure indicating the 3D grain structure of 2mm 2198T8R sheet material via EBSD (the crystal orientations are given with respect to the normal of each plane), (b) 2D section of 2198T8R from high resolution 3D X-ray laminography in the L-T plane and (c) Pole figure of 2198T8R.

including a cross-shaped 'shear to tension' (ST) as well as a shear only (SO) and a tension only (TO) geometry were designed and are shown in Fig. 2. The original shear sample geometry was miniaturized to be able to image the region of interest at micrometre spatial resolution by 3D synchrotron laminography imaging. A range of the dimensions of the region of interest (ROI), particularly the vertical and horizontal offsets between two hole positions, have been calculated and optimized by the finite element simulations. In the present work, all specimens were machined by the means of electrical discharge machining (EDM) from 2 mm raw sheet material of 2198T8R to 1 mm nominal thickness.

2.2.2. Mechanical in situ test

Experiments were performed using an *in situ* loading frame with a similar design as shown in [15]. It is presented in Fig. 3 where pin hole loading was applied. The cross-head displacement rate was 5 µm s^{-1}, which resulted in a strain rate of the order of 10^{-4} s^{-1} in the gauge section. Three kinds of experiments were carried out and noted as shear only (SO), tension only (TO) and 'shear to tension' (ST). Mechanical *in situ* tests were carried out for the ST sample in the horizontal LT plane, where shear loading was performed in the L and tensile loading in T so that the final crack was parallel to the rolling direction. Before the laminographic experiment, several proportional pre-tests (SO, TO) without laminography scanning were performed in the *in situ* machine. The entire database is given in [29].

2.2.3. Optical imaging setup for strain measurement in the region of interest (ROI)

In order to measure the deformation in the ROI of the sheet specimen with complex geometry (in particular enabling correlation of the experimental data with 3D FE simulations) and to prevent the deformation from being influenced by elastic deformation of the rig during the mechanical loading, an optical imaging setup was used to measure the surface displacements locally by DIC. To provide a suitable contrast for this, a fine random speckle pattern (average speckle size about 15 µm) was deposited on the specimen surface.

Surface images were taken with a sensor having 2048 × 2048 pixels (Basler acA2040 25g) in combination with different microscope optics, see Table 2, providing different spatial resolutions and related fields of view. During the laminographic *in situ* experiment, a surface image was acquired before each laminographic scan. In contrast, the surface image set of the

Table 2
Different optics and associated pixels sizes of the different experiments.

Microscopes group	Field of view (mm^2)	pixel size (µm/px)
SILL TZM 0420/3.0-C telecentric lens	3.85 × 3.85	1.875
Mitutoyo VMU-V microscope + 2× objective lens	5.43 × 5.43	2.65

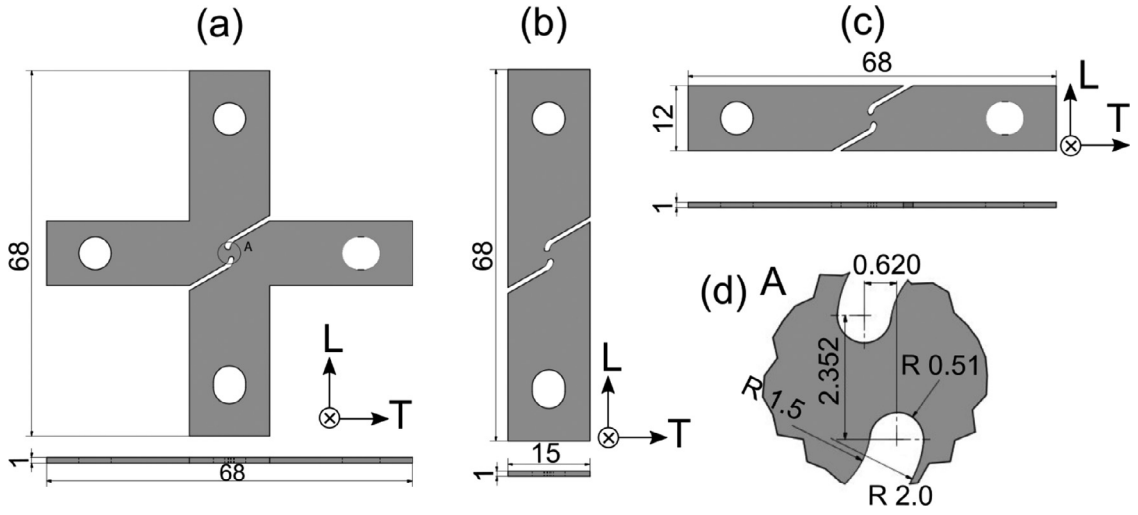

Fig. 2. Geometries of (a) Cruciform 'shear to tension' (ST) load path change, (b) Shear only (SO), (c) Tension only (TO) samples and (d) the detailed geometry of the region of interest (ROI).

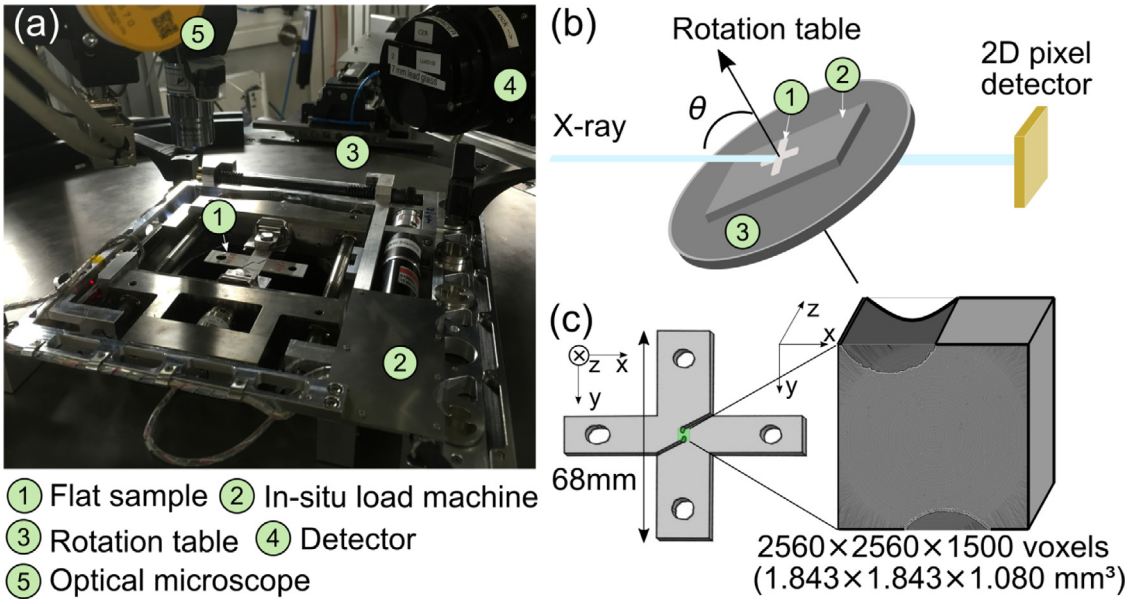

Fig. 3. Set-up for in situ laminography experiments: (a) ② loading frame rig with ① a cross-shaped sample on ③ laminographic table and the schemes of (b) laminographic stage and (c) 3D imaging region of interest (ROI) from the cruciform sample.

pre-tests conducted at the laboratory of Centre des Matériaux was continuously captured at a frequency of 2 Hz.

Macro measurement Instead of utilizing the local displacement of two points as in traditional extensometry, for uniaxial tensile experiments, a 4-point-frame optical extensometer illustrated in Fig. 4 was introduced to measure tension in both vertical and horizontal directions as well as the shear angle in ROI and to obtain an average macro measurement in the reference frame that could be compared with numerical computation.

From the surface DIC results of the optical images taken for each loading step, the relative displacement was calculated as the difference between initial positions and deformed positions using the four selected points. A general displacement field u inside the frame was generated from bi-linear interpolations.

According to the specific geometry, the region of interest was mainly under a simple shear state, which was a composition of pure shear and rigid body rotation. The deformation gradient F_{ij} was the derivative of the deformed configuration position vector x_i with respect to the reference configuration position vector X_j [30].

In order to remove rigid body rotation, **F** can be written by using the polar decomposition as the product of two tensors: a rotation tensor **R** and a symmetric right stretch tensor **U**.

$$F_{ij} = \frac{\partial x_i}{\partial X_j} = R_{ik} \cdot U_{kj} \tag{1}$$

Tension stretch along x axis U_{11} and the absolute value of shear stretch U_{12} were chosen as the tensile and shear measurements respectively.

$$\mathbf{U} = \begin{bmatrix} U_{11} & U_{12} \\ U_{12} & U_{22} \end{bmatrix} \tag{2}$$

Accumulated equivalent strain measurement During the complex non-proportional loading path damage was accumulated. The definition of a suitable accumulated strain that can be related to the damage state was important so as to estimate strain to fracture. As other works indicated [10,31], the logarithmic strain (Hencky strain or true strain) takes into account the influence of the strain path

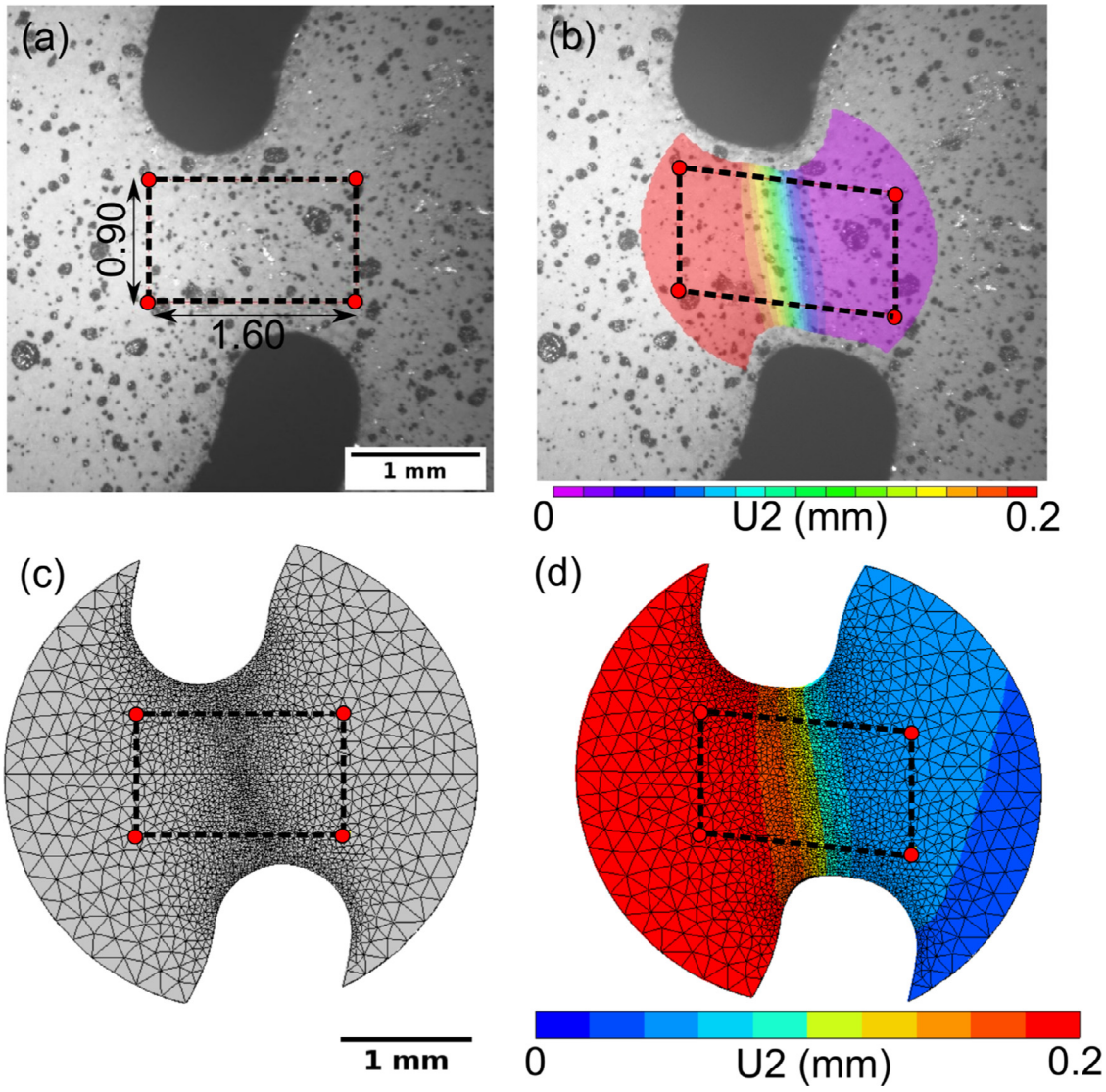

Fig. 4. 4-point-frame visual extensometer on (a) reference and (b) deformed images for image correlation and the same 4-point-frame were chosen in (c) initial and (d) deformed steps from the finite element model to synchronize experiment and simulation.

and is defined as:

$$\varepsilon = \frac{1}{2}\log\left(\mathbf{F}^T \cdot \mathbf{F}\right) \tag{3}$$

This expression provides an appropriate measure especially for large simple shear strain [32,33].

Equivalent strain needs to be cumulative to estimate an effective strain during the load path change. The work-conjugate equivalent strain is defined in terms of the adopted constitutive model [34]. However, considering the complexity of the anisotropic model, an accumulated equivalent von Mises strain has been applied to the total strain tensor in the following as [31] :

$$\varepsilon_{\text{cum}} = \int \sqrt{\frac{2}{3} d\varepsilon : d\varepsilon} \tag{4}$$

Besides, Butcher and Abedini pointed out that the difference between the equation and the work-conjugate definition for a von Mises behavior remains negligible when strain is less than 0.8 [34]. The same strain definition was applied here for the DIC data and for the FE simulation results to have comparable fields during the non-proportional loading. The equation in Eq. 4 satisfies all the requirements.

Moreover, due to a lack of information in the thickness direction (S) in experimental 2D surface image correlation, the third component has been calculated from a plastic incompressibility assumption $\varepsilon_I + \varepsilon_{II} + \varepsilon_{III} = 0$. Hence, the accumulated equivalent strain increment is computed as:

$$\Delta\varepsilon^{\text{2d}}_{\text{cum}} = \sqrt{\frac{2}{3}\left(\Delta\varepsilon_I^2 + \Delta\varepsilon_{II}^2 + \Delta\varepsilon_{III}^2\right)} = \frac{2}{\sqrt{3}}\sqrt{\Delta\varepsilon_I^2 + \Delta\varepsilon_{II}^2 + \Delta\varepsilon_I\Delta\varepsilon_{II}} \tag{5}$$

2.2.4. Non-proportional in situ synchrotron laminography experiment

The *in situ* mechanical experiment, a non-proportional loading 'shear to tension' (ST) test, was carried out at the beamline ID19 [35] of the European Synchrotron Radiation Facility (ESRF, Grenoble France). During the experiment, the shear loading was applied and unloaded before turning the cruciform sample by 90 degrees and loading it in tension. Tensile loading was applied until final fracture, shown in Fig. 7. 24 scans were performed with a stationary X-ray beam with the sheet thickness direction (S) being inclined at an angle of 60° with respect to the X-ray beam axis in Fig. 3. An indirect detector system was employed, composed of an approx. 10 μm thick Eu-doped gadolinium gallium

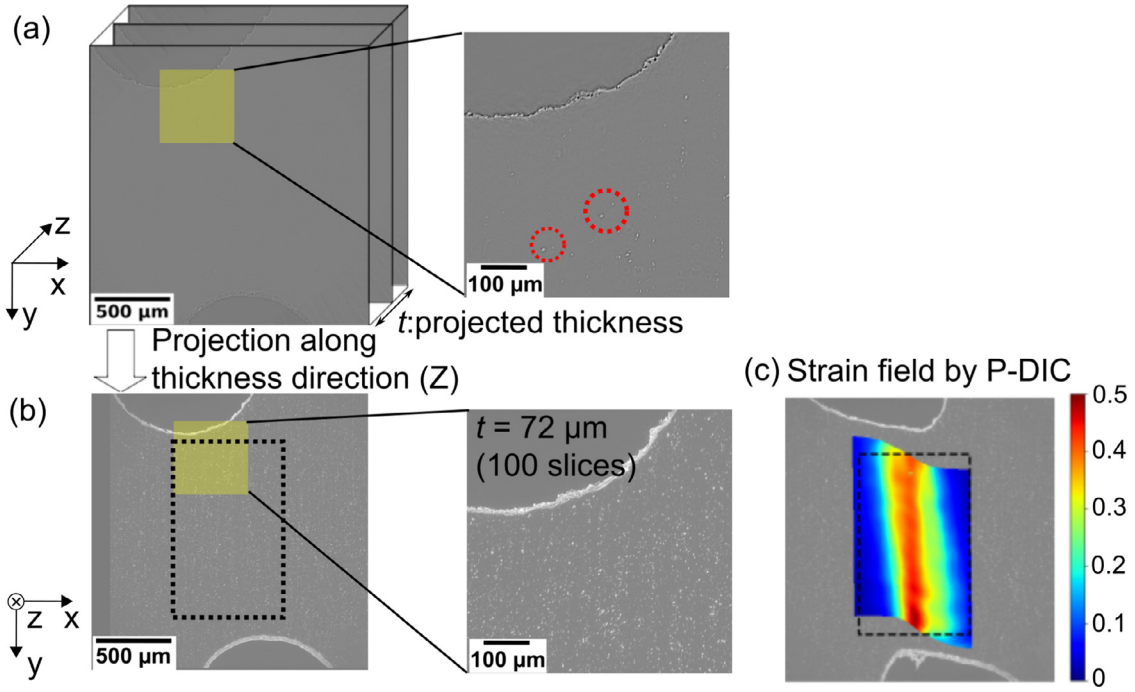

Fig. 5. (a) Stack of 100 individual reconstructed cross sections from the 3D volume data with limited constrast have been projected to (b) an image with sufficient contrast using the maximum grey level. (c) The strain field is obtained via 2D image correlation of such projected images (of the 72 µm thick slice) before and after each loading step.

garnet thin-film scintillator optically coupled via microscope optics suitable for high-dose imaging [36] and 9× effective magnification to a scientific camera (pco.edge 5.5, PCO, Kehlheim, Germany). For each scan, a series of 3600 radiographs was acquired with an exposure time of 40 ms for each projection direction at an X-ray energy of approximately 35 keV. The 3D data was reconstructed utilizing a filtered-back projection algorithm [37] to a size of 2560 × 2560×1500 voxels with a physical length 0.72 µm/pixel, thus the corresponding physical volume in the material bulk was around 1843.2 × 1843.2 × 1080 μm^3 as shown in Fig. 3. The parameter optimization for the 3D reconstruction was performed automatically using a GPU-accelerated implementation of this algorithm [38]. Due to unforeseen instrumentation problems, the volumes of the last two steps were acquired at a lower resolution with a physical length 1.44 µm/pixel after some hours of mechanical stress relaxation.

2.2.5. 3D image analysis

To segment damage, a region growing algorithm [39] was used. It was chosen to project the damage on one surface to obtain a surface void fraction rather than a void volume fraction, as will be discussed later. The surface on which the damage was projected was the future fracture surface (projection approximately along T direction over a length of 144 µm). The surface void fraction was computed as number of pixels that belong to the segmented projected damage divided by the number of pixels of the total area.

2.2.6. Digital image correlation analysis

We used the commercial DIC software *Vic2D-6* (Correlated Solutions) to correlate 2D surface images and 3D volumetric images taken at every load step to obtain displacement and strain fields at the selected ROI.

Surface DIC Images taken by the camera of the optical imaging setup at different loading steps have been used to correlate and generate the displacement and strain fields on the specimen surface. Subset size and step size were set as 55 pixels (146 µm) and 5 pixels (13 µm) respectively in Vic-2D for the laminographic tests while 55 pixels (103 µm) as subset size and 10 pixels (19 µm) as step size for the other pre-tests. All highly deformed (i.e. shear) and load path change tests were conducted with incremental correlation. Hencky strain was computed with a filter size of 15. The surface displacement fields are used here to compute the stretch via the 4-point-frame extensometer.

Projection DIC On account of the low particle volume fraction in this material, it was difficult to calculate reliable digital volume correlation data from the limited contrast in the reconstructed 3D images. Generally, single slices of laminographic 3D volume data exhibit an insufficient density of natural markers for correlation. A technique called projection DIC (p-DIC) has been applied in [10,11,14,15] where contrast (for example using a maximum or a minimum norm), contained in several cross sections of the 3D volume data were projected along the thickness direction into one image. The contrast of white intermetallic particles contained in a 100 voxel (i.e. 72 µm) thick slice around the sample middle plane was projected on a 2D plane in Fig. 5. The projected 2D images for each load step could be correlated to determine the in-plane component of displacement and strain fields. Note that meaningful results were only obtained with this technique under the absence of strain field gradients (inside the projection volume of the chosen slice) along the specimen thickness direction. The onset of damage can be a problem for DIC as the hypothesis of conservation of contrast is no longer satisfied. For the present p-DIC approach this is not a major problem as the white particles (maximum grey value) are projected. In contrast, the damage is dark and does thus hardly affect the final 2D image. Only the edges of the crack, that are bright due to the phase contrast, affect the projected image, but this has not been a problem for the current correlation. Compared to digital volume correlation, this technique was more robust and saved computation time. Subset size and step size were set as 95 pixels (68.4 µm) and 10 pixels (7.2 µm) respectively in Vic-2D and incremental correlation was used. The results were exported as csv files and post processed to compute the accumulated

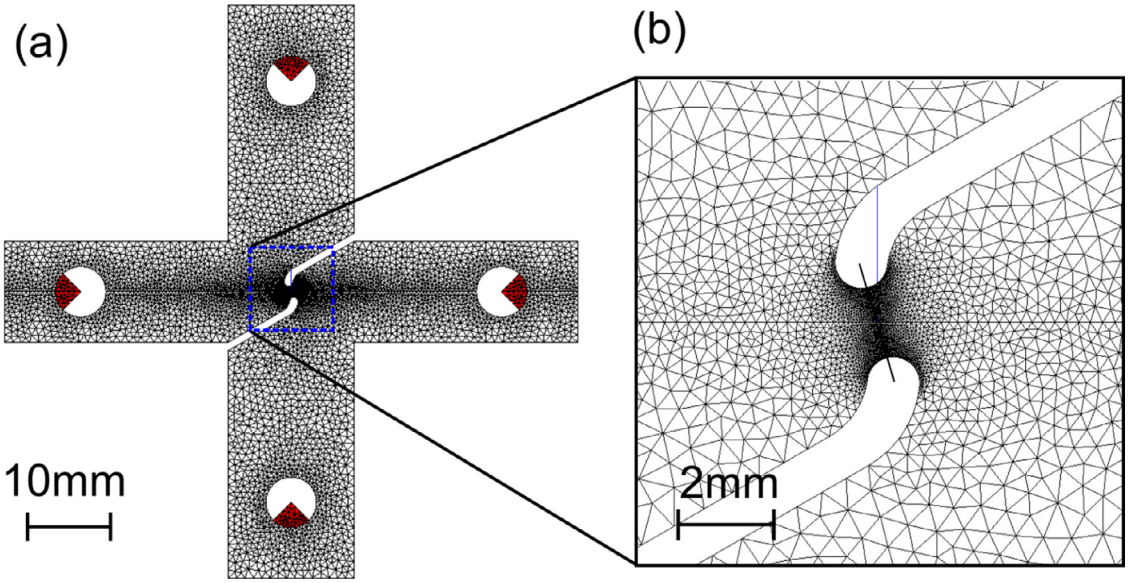

Fig. 6. Finite element mesh of (a) cross geometry where the elements of supports are in red. (b) Region of interest (ROI) of the geometry with mesh size down to 30 μm. (For interpretation of the references to colour in this figure legend, the reader is referred to the web version of this article.)

equivalent strain via Python according to Eq. 5, the field of which is shown under deformed frame in Fig. 5 (c).

3. Computational model

The finite element method was used to estimate the stress state (e.g. access to stress triaxiality) and to obtain the accumulated equivalent strain to fracture inside the material bulk so as to compare with experimental results. All simulations were performed using the finite element software Z-set [40].

3.1. Numerical finite element model

Due to the symmetry of the specimen's geometry, half of its thickness was meshed using the reduced integration quadratic tetrahedral element (c3d10R). A mixed displacement-pressure updated Lagrangian formulation was applied for the tetraedral element to account for large plastic strain and incompressibility especially for the micro specimen series ([41,42]). The element size varied from 30 μm to 100 μm, as illustrated in Fig. 6. Pins were modelled as elastic steel (red part) to apply the tensile load to the specimen.

The experimentally-measured global displacement rate was set to the order of 10^{-4} s^{-1} on the pins. In order to remove the machine compliance effect, local shear stretch U_{12} and tensile stretch U_{11}, as calculated from the deformation gradient **F** using the 4-point-frame visual extensometer, were chosen to synchronize experiment and numerical simulation.

3.2. Material behavior

Aluminium alloy 2198T8R has been modelled using a Chaboche-like [43] elasto-plastic behaviour with isotropic hardening. Bron-Besson's yield criterion was applied to account for plastic anisotropy [44]. The parameters have been calibrated with tensile test results of differently notched samples tested in different loading directions and more results are discussed in [29].

4. Results

4.1. Macroscale measurement: nominal stress-stretch curves

In order to remove deformation due to sample and machine stiffness, the 4-point frame visual extensometer described in Section 2 was used for a local measurement of shear stretch U_{12} and tension stretch U_{11} in the ROI. Fig. 7 shows the curve of the nominal stress (force F divided by the initial area of minimum cross section S_0) versus shear stretch U_{12} or tension stretch U_{11}. In Fig. 7 (a) the result for a representative monotonic shear only (SO) experiment is given as black dots together with the shear part of the *in situ* laminography 'shear to tension' (ST) load path change experiment as red triangles. Unloading was performed at about half the shear stretch to fracture of the SO experiment. Fig. 7 (b) shows the result for a representative tension only (TO) experiment as black dots together with the tension part of ST load path change result as red triangles.

The proportional loading SO experiment showed a shear stretch to fracture of $U_{12}^{f_{SO}} = 0.135$ within a range from 0.132 to 0.137 found by repeated testing [29], see Fig. 7 (a). At least three tests were performed to obtain the average strain to fracture values [29]. A maximum nominal stress of about 325 MPa was reached. The shear part of the non-proportional load path change ST showed a very similar nominal stress-stretch curve to that of the SO experiment. Unloading of the shear to tension load path change was carried out at a shear stretch U_{12} around 0.08. The monotonic TO test shown in Fig. 7 (b) reached nominal stresses of about 515 MPa and an average tension stretch at fracture of about 1.117 was found. The scatter in stretch to fracture from repeated testing was found in a minimum-maximum range from 1.105 to 1.130 [29]. During the ST load path change test, the tension stretch U_{11} started with an initial shift of 0.025 on the tension curve as there was a slight tension stretch during shear loading. After this shear loading, a higher nominal stress at yielding was found compared to a proportional test, which was due to hardening during the shear loading without necking. The tension stretch to fracture in tension after shear was $U_{11}^{f_{ST}} = 1.104$, which was less than the average tension stretch to fracture of a tension only test. Thus, the average tension stretch to fracture of shear followed by tensile (ST) loading

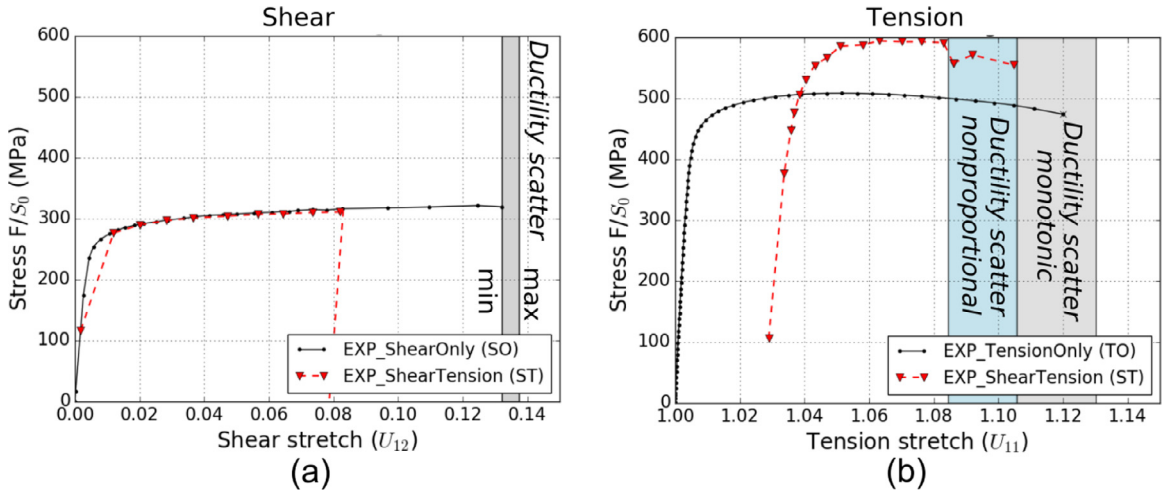

Fig. 7. The curves of nominal stress versus (a) shear stretch U_{12} and (b) tension stretch U_{11} for two proportional loading Shear-Only (SO), Tension-Only (TO) tests as well as non-proportional loading 'shear to tension' tests. S_0 stands for the initial cross surface in region of interest (ROI).

($U_{11}^{f_{ST}} = 1.098$) was 16% reduced compared to that of proportional TO loading ($U_{11}^{f_{TO}} = 1.117$). Here, if the tension stretch during shear pre-loading was not taken into account, this reduction would be even higher. A detrimental effect of the shear loading before tension on the stretch to fracture during tensile loading can clearly be identified. The origin of this detrimental effect in terms of damage micro-mechanisms is studied in the sequel.

4.2. Mesoscale analysis of strain and damage fields

This section focuses on the mesoscale analysis of strain fields, damage and stress states. The nominal stress versus stretch curve of the shear to tension load path change test is given in Fig. 8 and the instances at which a scan was performed are shown. The simulated curve is also plotted. First, the equivalent accumulated strain fields at load increments of the 'shear to tension' test are shown for FE computations as well as for 2D projection DIC results from synchrotron laminography 3D data. The segmented damage from synchrotron laminography 3D data is shown for the 'shear to tension' LPC and compared with strain fields. Moreover, the stress state was assessed using FE where the stress triaxiality fields in the region of interest have been analysed for different loading increments. Last, the segmented damage has been quantified as surface void fraction by its projection on the future fracture surface during the non-proportional load path change.

4.2.1. Equivalent accumulated strain and damage fields

The accumulated strain fields were obtained with two different techniques: projection DIC from experimental 3D laminographic volume data and from FE simulations. In order to further assess the interaction of strain localization and damage evolution from shear to tension, the results during load path change were investigated and divided into three main periods: shear loading period in Fig. 8, tension elastic loading period in Fig. 9 and tension plastic loading period in Fig. 10. For selected load steps in Fig. 8, 9 and 10, the strain evolution in the highly strained middle plane region is given for the 'shear to tension' load path change. Simultaneously, the segmented damage fields were investigated in a volume (1100 × 1600×1000 voxels representing 792 × 1152×720 μm^3 shown in yellow in Fig. 8 (c)) of 3D laminographic data and are given in column (e) as top views, normal to the sheet plane, and in column (f) views normal to the shear plane at selected load steps indicated by the numbers in circles.

Shear loading period (steps 0–9) During shear loading, a similar shear band shape and amplitude of strain fields was found when comparing projection DIC and FEA in Fig. 8 (d)(g) respectively. The highly-strained shear band was situated along the line linking the two blunt notches. At the end of shear loading (step 9), the maximum equivalent accumulated strain measured by projection DIC reached up to 0.45 in shear band near the notches. Fig. 8 (e)(f) at the end of shear, at step 9, shows damage that nucleated and grew under shear. Such damage is commonly not expected as it is generally assumed in the literature that hydrostatic pressure is needed for damage to evolve [1] whereas here straining occurred and localized in the region where stress triaxiality was close to zero. Damage features including large flat cracks and cracks within intermetallic particles were observed and were distributed uniformly through sample thickness during shear loading.

*Tension elastic loading period (step 10–16)*After unloading of the shear sequence, the sample was turned by 90° and a tensile load was applied to the cruciform sample. The mesoscopic effect resulting from this operation are shown in Fig. 9. The maximum strain value in the shear band only increased slightly due to the small elastic strains occurring during unloading and reloading. At the end of tension elastic domain (step 16), there was no hidden shear crack opening seen from segmented damage views in Fig. 9 (b)(c) compared to those at the end of shear. Closed and invisible shear cracks might have been present during shear as the hydrostatic pressure was lacking to open them and make them visible in 3D imaging. This does not seem to be the case.

Tension plastic deformation sequence (step 17–24) Fig. 10 shows the strain and damage evolution during plastic deformation in tension up to final fracture. The shear band became wider under tensile loading and the measured equivalent accumulated strain increased up to 0.5 at the last step; number 24. With the onset of plastic deformation in tensile loading, the nucleated damage during shear loading continued to grow. Small damage features and large flat cracks could be distinguished. Subsequently the damage features coalesced into cracks that led to final failure along the shear band region in Fig. 10 (b)(c). During the last step before fracture (step 24), these damage features all grew very fast and coalesced into flat damage clusters. Damage evolution was mainly seen in the highly strained regions. The damage nucleated in shear loading may explain the reduction in ductility during tensile loading in Fig. 7 (b) compared to the proportional tension only test. The microscopic damage features evolution will be focused on in more detail in later sections below.

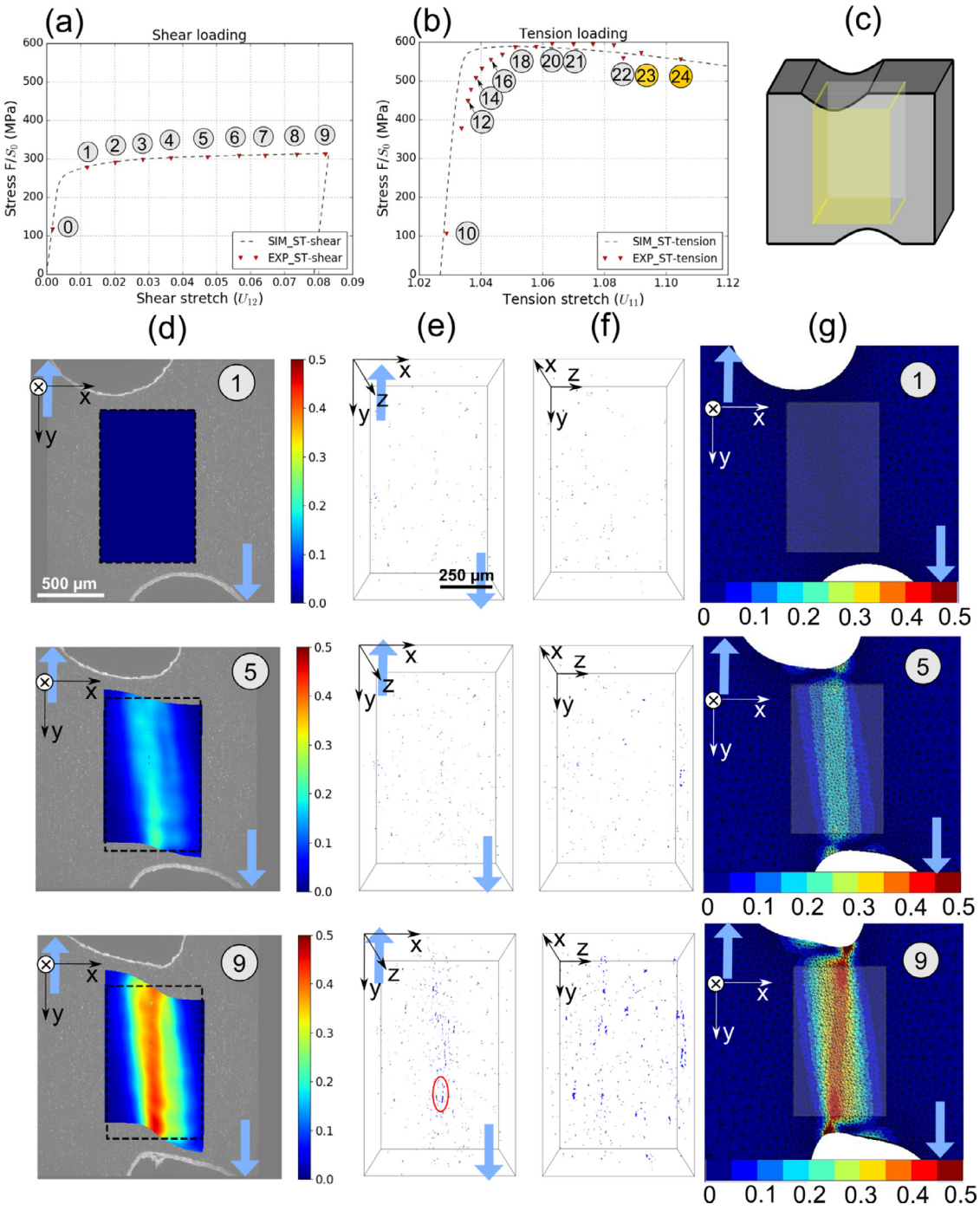

Fig. 8. The experimental and simulated nominal stress versus stretch curves for (a) shear to (b) tension loading. (c) ROI location. Shear loading sequence: Accumulated equivalent strain fields on the middle plane in the ROI via (d) laminography data based p-DIC (72 µm deep projection along *Z* axis) and (g) FEA. Segmented damage visualizations of *in situ* laminography data (c) yellow ROI (1100 × 1600×1000 voxels) from (e) X-Y plane and (f) Y-Z views during shear loading period from 'shear to tension' (ST) load path change. (For interpretation of the references to colour in this figure legend, the reader is referred to the web version of this article.)

Fig. 11 shows the strain profile along a horizontal line normal to the shear band for both (a) FEA and (b) projection DIC results. Here different colours represent different loading steps where FEA is shown as dashed lines and projection DIC as full lines in (c). The maximum strain level and distribution show good agreement between experiment and simulation. During shear loading, the maximum strain along the horizontal line increased from 0 to 0.4. When turned to subsequent tensile loading, maximum strain continued to increase up to 0.55 for FEA results and 0.48 for projection DIC at step 24 since the highly deformed images were not correlated by DIC for the last 2 steps. The projection DIC strain profile exhibits a second peak, which could be linked to a crystallographic effect (cf. grain size) considering its length.

4.2.2. Stress state

Thanks to FE computations, the stress state during this non-proportional load path could be evaluated. The stress triaxiality

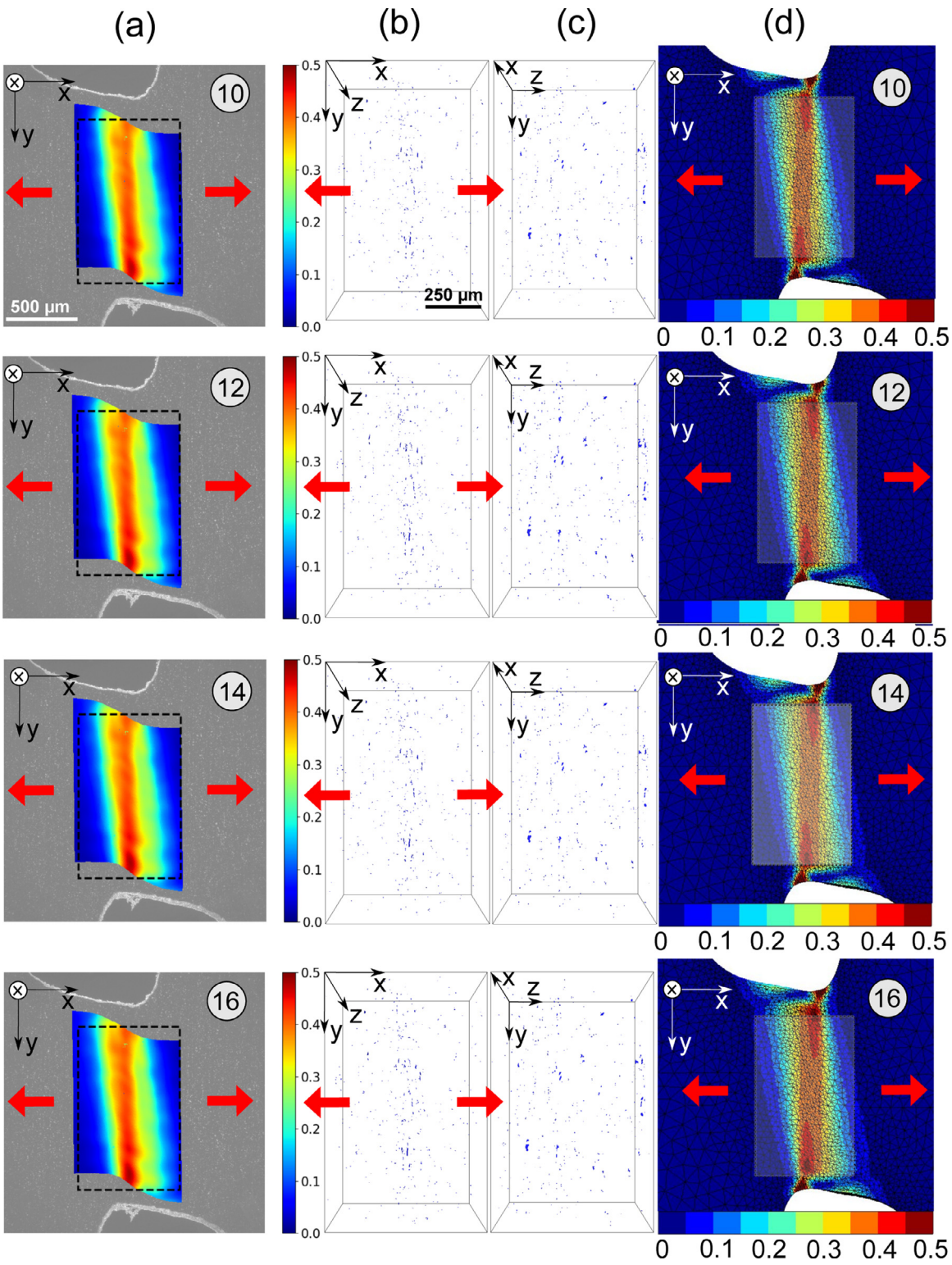

Fig. 9. Elastic part of the tensile loading sequence: Accumulated equivalent strain fields on the middle plane via (a) laminography data based p-DIC (72 µm deep projection along *Z* axis) and (d) FEA. Segmented damage visualizations from *in situ* laminography data (b) X-Y plane and (c) Y-Z views during tension plastic period from 'shear to tension' (ST) load path change.

(mean stress divided by equivalent stress) distribution was analysed along two lines normal to the shear band at both the surface plane and middle plane in Fig. 12 (a) and (c). In Fig. 12 (b) and (d) the stress triaxiality profile along the shear band, i.e. in *Y* direction is shown. During the shear loading (blue), stress triaxiality along the shear band was near zero (between −0.1 and 0.05) for all curves, as intended. During subsequent tensile loading, the stress triaxiality increased to values from 0.4 to 0.6 at the middle plane whilst it decreased from 0.66 to 0.4 on the surface plane in Fig. 12 (a)(b). Thus, the middle plane was under higher stress triaxiality during the tensile loading where high strain was encountered in Fig. 12 (c)(d).

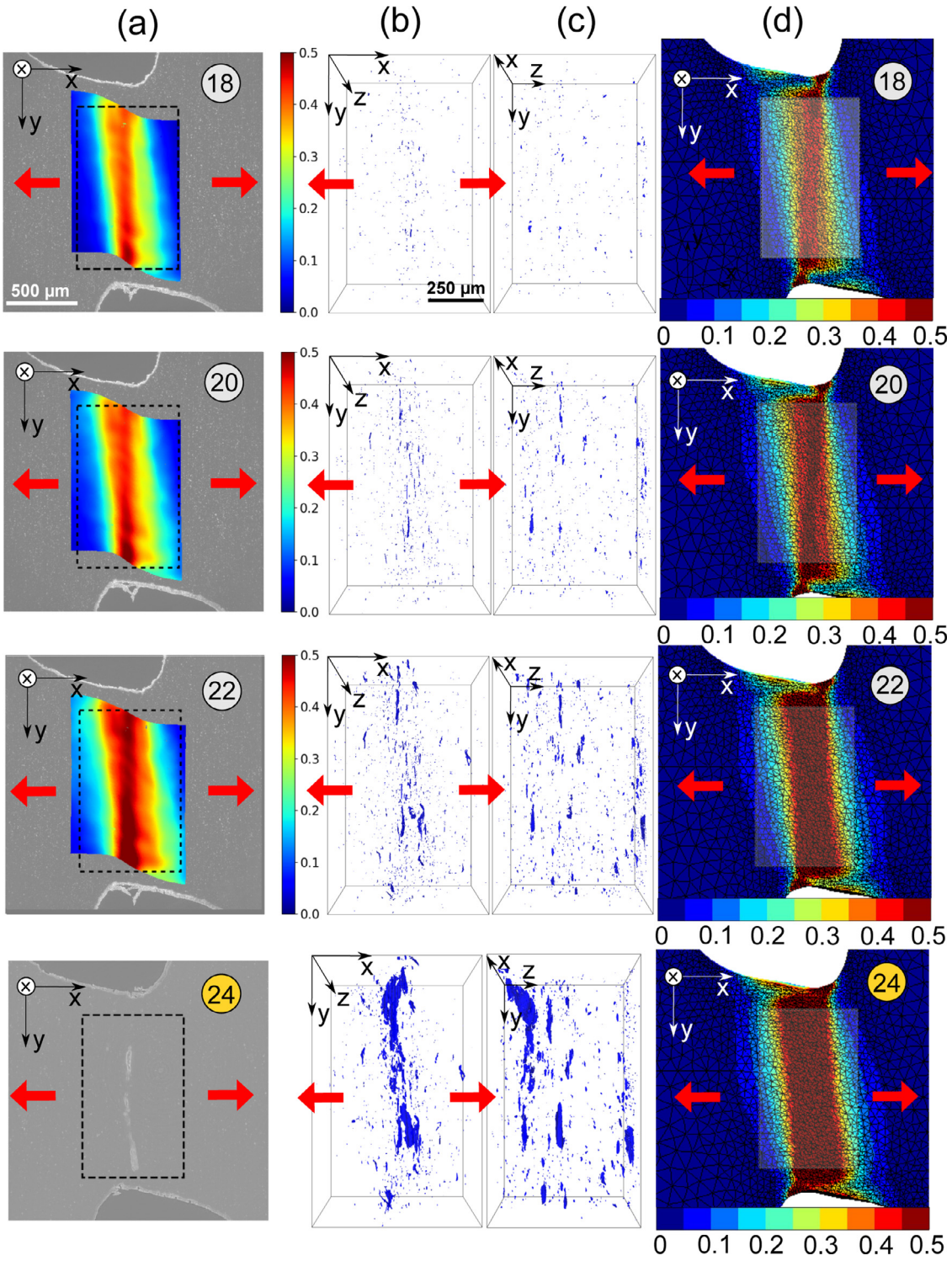

Fig. 10. Plastic deformation part of the tensile loading sequence: Accumulated equivalent strain fields on the middle plane using (a) laminography data based p-DIC (72 µm deep projection along *Z* axis) and (d) FEA. Segmented damage visualizations from *in situ* laminography data (b) X-Y plane and (c) Y-Z views during tension-plastic period from 'shear to tension' (ST) load path change.

4.2.3. Damage quantification and analysis

Fig. 13 (a) shows the raw volume data of 2560 × 2560×1500 voxels that were imaged by 3D synchrotron laminography. In order to focus on the region of interest where damage developed, the raw volume was cut into a smaller volume with a size of 1100 × 1600×1000 voxels. Using a region growing algorithm [39], the damage (black) was segmented from aluminium matrix (grey) in Fig. 13 (b). It was chosen to project the damage on one surface (fracture surface) as the flat cracks are more detrimental than voids but have a very low void volume fraction. This is why the surface void fraction measurement seems to be more relevant in evaluating the damage progression. A ROI (green) was selected where the

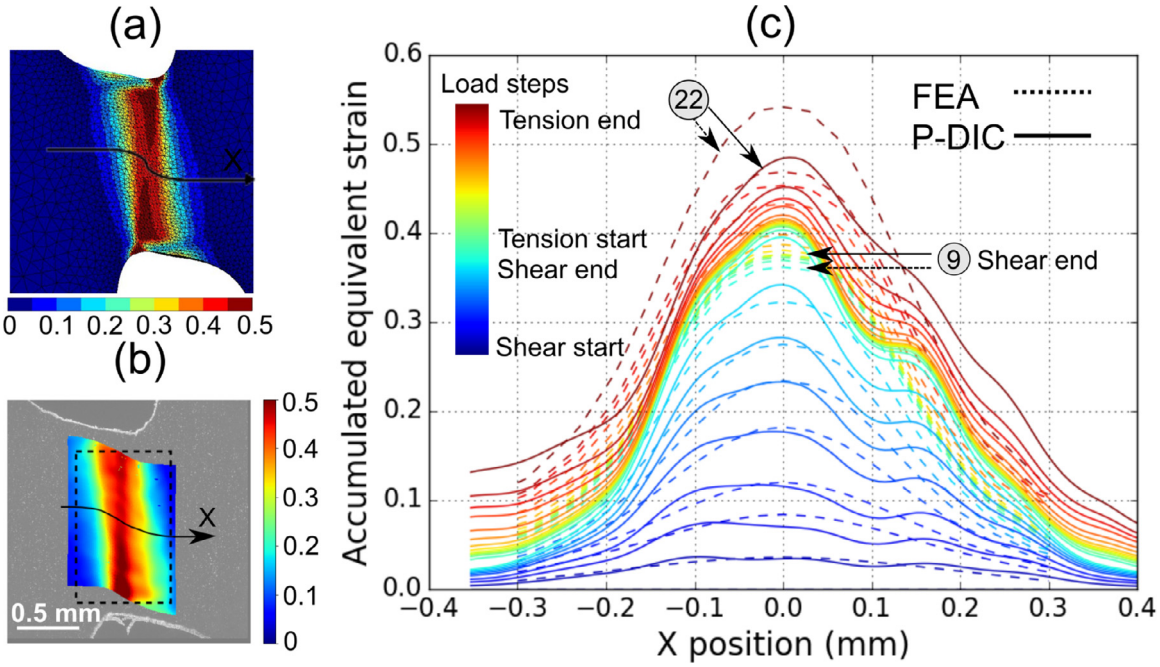

Fig. 11. a) Indication of the horizontal profile line (*X*) for (a) FE and (b) for projection DIC along which the accumulated strain profiles (c) were obtained during 'shear to tension' loading by projection DIC (full line) and via FE analyses (dashed line).

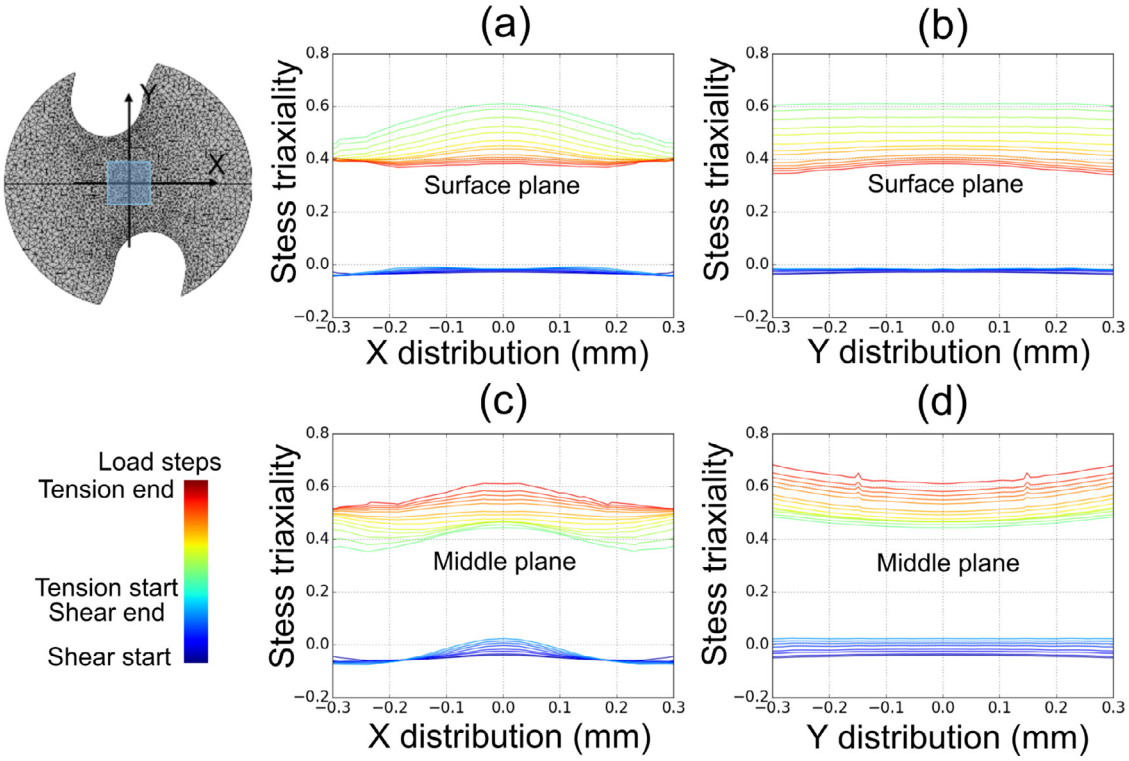

Fig. 12. Stress triaxiality distributions along the horizontal line *X* axis and vertical line *Y* axis from shear load to tension at (a)(b) surface plane and (c)(d) middle plane from FEA calculation.

damage along *X* axis (200 pixels = 144 μm) was projected on the future fracture Y-Z surface (yellow) as shown in Fig. 13 (b) and binarized as surface void fraction in Fig. 13 (d).

The damage evolution was quantified as surface void fraction versus equivalent accumulated strain from the p-DIC profile (last two points with dashed line are FE results) shown in Fig. 13 (e) during the 'shear to tension' non-proportional loading. The surface void fraction grew steadily till the end of shear where voids and flat cracks were observed. A void surface fraction of about 1% was found at the end of shear. Then a slight decrease of void fraction was subsequently seen due to unloading followed by tensile elastic loading which closed some voids. Finally the damage surface fraction increased with a higher slope up to 4% and then substantially up to 11% during tension until reaching fracture. Please remember the damage evolution of the last two points was obtained from the scans at lower resolution and are therefore underestimated be-

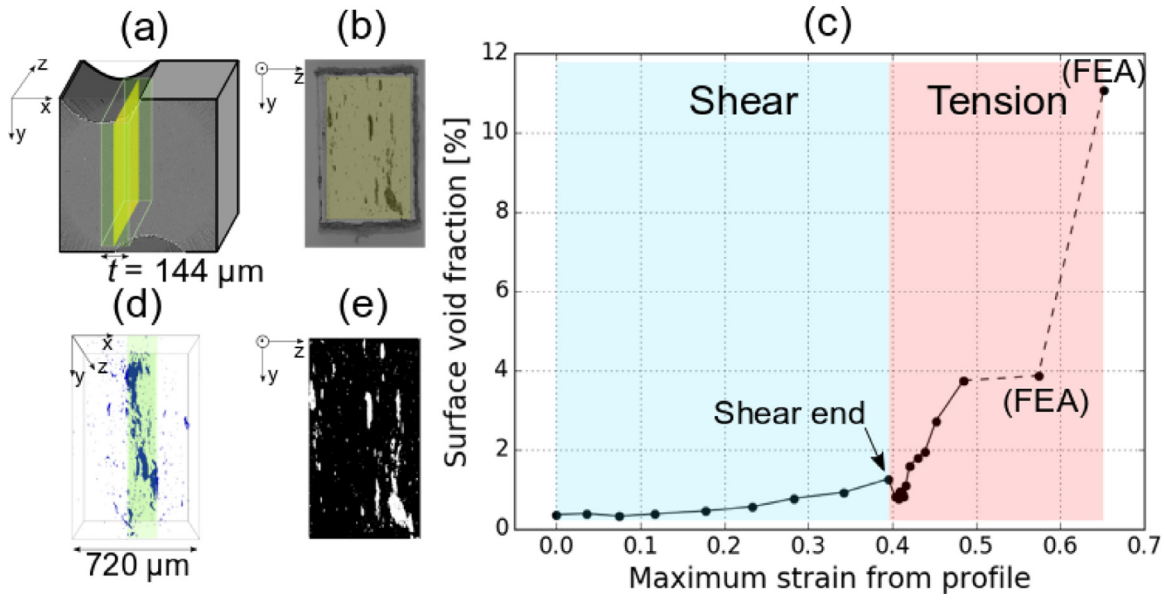

Fig. 13. Damage quantification: (a) and (b) schematic representation of the green ROI in the scanned volume for damage surface fraction measurement, (d) Segmented damage inside green ROI from laminography volume data is projected along the *X* axis (144µm) on the yellow 2D plane shown (b) and in (e), (c) measured surface void fraction versus accumulated equivalent strain during the 'shear to tension' load path change while the strain of the last two points were from FE and their void fractions from lower resolution scans. (For interpretation of the references to colour in this figure legend, the reader is referred to the web version of this article.)

cause some damage features were not able to be captured at the lower resolution.

4.3. Microscale: Damage micromechanisms

After mesoscale damage quantification during the non-proportional load path change, a deeper investigation of damage mechanisms is shown here via the high resolution 3D imaging data acquired. Two main damage features were found and focused on: flat cracks and damage linked to nucleation of voids on intermetallic particles. These features were tracked during the laminographic experiment from shear to tension loading.

4.3.1. Flat crack

One of the flat cracks is visualised in Fig. 14 (a) and can be followed during the loading in (d). The minimum grey value in the selected region was projected along the thickness direction *Z* axis to obtain a surface projected damage image of 400 pixels × 200 pixels (288 × 144 μm^2) shown in Fig. 14 (b). The projected damage images were observed and tracked from shear to tension in Fig. 14 (d). Three flat cracks were first observed at step 5 and they grew slightly with shear loading. These features did not nucleate on intermetallic particles. The size in terms of length and width of these cracks resembles the typical grain size. The cracks could be intergranular or transgranular. Subsequently the cracks opened under tensile loading. They started to coalesce at step 18 and finally led to a long flat crack. The three-dimensional evolution of the flat crack is shown in Fig. 14 (c) where different colours represent different loading steps. It can be seen that the damage growth and coalescence is a continuous process. The crack first nucleated and then grew during shear. Under subsequent tension loading it further grew and different crack parts coalesced.

4.3.2. Intermetallic particle crack

An intermetallic particle of 30 µm × 10 µm size was tracked in Fig. 14 (e). During shear loading, the particle rotated from 26° to −25° with respect to the horizontal line and a fracture within the particle was formed the orientation of which was normal to the principal stress direction at end of shear (step 9) which had already been observed in [11]. Also a vertical crack was seen at the end of shear loading. During unloading the crack closed to some extent. They subsequently reopened and grew under tensile loading. This was particularly seen for the vertical crack.

5. Discussion

A detrimental effect of the shear pre-loading before tension was clearly identified in the present study. The tension stretch to fracture was reduced by about 20% compared to proportional loading at the macroscale. On the one hand, the nominal tensile stress after shear pre-loading hardening increased by 20% up to 600 MPa. A higher stress level could contribute to ductility reduction. On the other hand, it was also shown that shear-dominated loading already led to damage nucleation and growth even though the stress triaxiality was close to zero. This induced damage can explain the ductility reduction.

The damage of an aluminium alloy AA2024-T3 under shear loading was investigated via synchrotron X-ray laminography in [11]. Particle cracking as a damage nucleation mechanism was also found in that study but no flat grain-related cracks were found. The flat cracks are believed to be more detrimental for aluminium alloy 2198-T8R whilst intermetallic particles and pre-existing voids play a minor role. The flat cracks are probably linked to the material grain structure considering the crack length and width that are around several tens of micrometers. These flat cracks that nucleated under shear subsequently grew and coalesced to final cracks under tension shown in Fig. 14 (d). Similar cracks have also been found for this material in tension loading [26]. For this material in T3 condition a crack nucleated in tension was shown to be transgranular [39].

Previous shear-dominated damage mechanism studies almost all focused on the void-mediated failure (i.e. void nucleation-rotation-elongation) [10,20]. However, for an alloy with very limited initial porosity or pre-existing voids, the void-mediated damage mechanism is not likely to govern the failure and the origin of the detrimental flat cracks deserves further exploration. This also

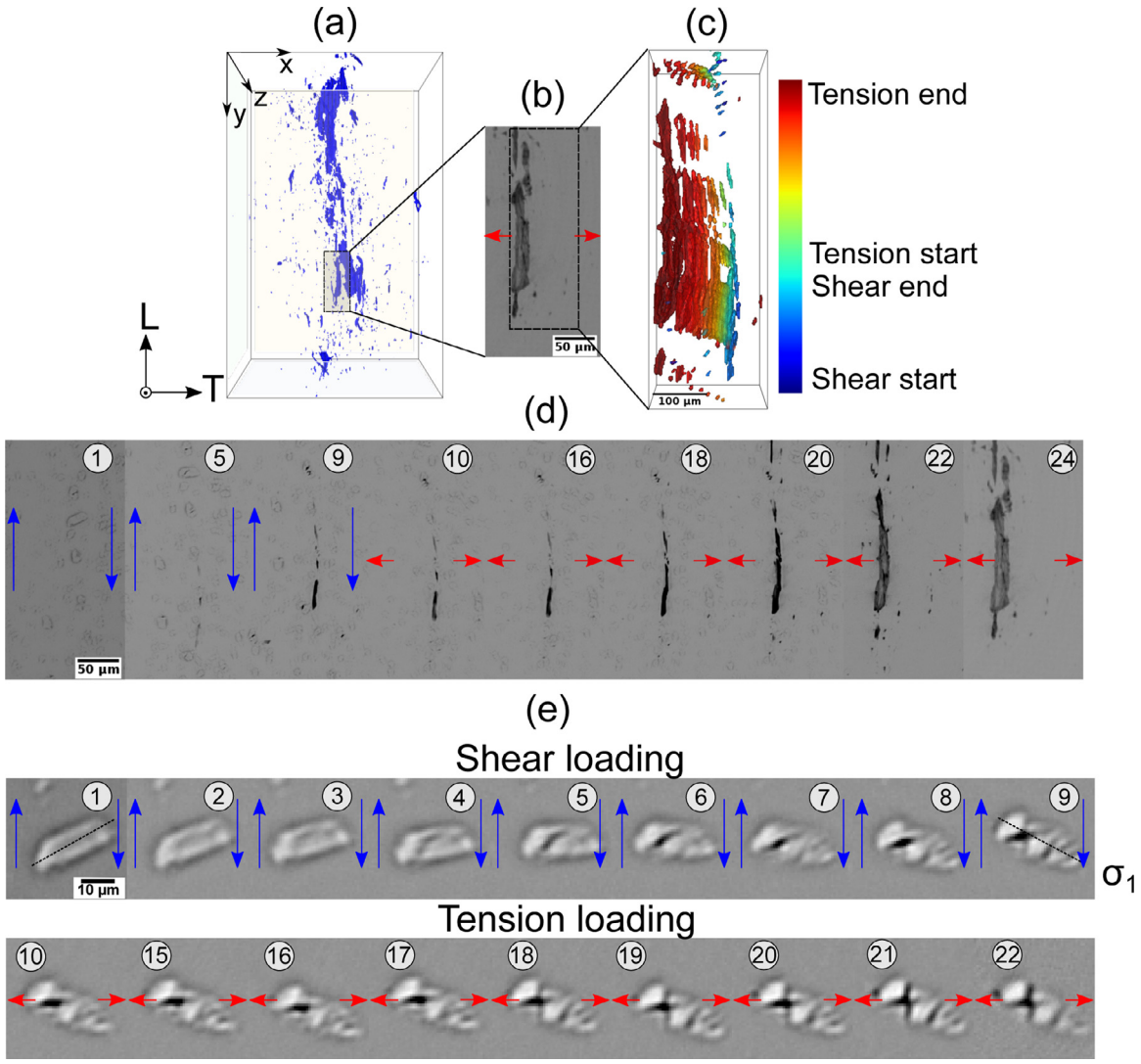

Fig. 14. (a) Damage visualization of laminography data in the shear band region at final load step 24 before fracture where (b) one of flat cracks was tracked. (c) Local 3D damage visualization of the tracked flat crack, shown in (b), with different colours representing loading steps from shear to tension. Damage view of two typical damage features: (d) flat crack, shown in (b), evolution studied by minimum grey value projection along 100 voxels and (e) single section of the evolution of an intermetallic particle during nonproportional 'shear to tension' loading.

highlights the effect of microstructure on damage mechanisms in shear that should be investigated.

Furthermore, the damage mechanisms under load path changes are even more complex. Bruenig et al [4] studied the remarkable effect of shear preloadings to a different extent (45%, 65% and 90%) on the ductility under tension loading. The fracture displacement of different shear preloadings was significantly reduced with that compared to proportional tensile loading. In the SEM observation of the samples that were pre-loaded in shear to 90% of the failure displacement, micro-shear-cracks were observed on fracture surfaces and are supposed to have accumulated as macro-cracks in the subsequent tensile loading. Using the advanced technique synchrotron laminography, the damage evolution could be further analysed at high resolution during load path change in terms of micro damage mechanism.

The current µm-resolution was not sufficient for a detailed study of the nucleation of flat crack features under shear loading. Synchrotron nanolaminogrpahy was successfully applied to study ductile damage for tensile loading [45], which allows a three-dimensional insight in flat sheet specimens at voxel sizes down to 50 nm. The formation of flat cracks and intermetallic particle cracks features could be observed at a very early stage and the damage micro-mechanism under shear loading should be better studied and understood.

A similar methodology as in the present study could be applied to other load path changes: 'tension to shear'. With 3D synchrotron laminography, the shear damage mechanism under non-proportional load path changes would be better understood up to fracture. In this study, an anisotropic elasto-plastic material model was applied. In order to better predict damage and failure under different non-proportional load path changes, a suitable damage model is needed. Current models under shear-dominant loading [10,20] assume the shape changes of pre-existing voids or decohesion of rigid particle rather than void nucleation without the presence of particles.

A fully coupled classical void damage at high stress triaxiality and Coulomb model at the slip system scale at low stress triaxiality based ductile fracture model [46] could also be applied to predict the present data of non-proportional load path changes. A reduced texture methodology (RTM) was used to provide computa-

tional efficiency and this approach involved a significant reduction of the number of representative crystallographic orientations. The damage nucleation along slip planes could represent the observed generation of shear cracks.

6. Conclusions

An *in situ* laminography multiscale experiment was carried out to study the deformation and ductile damage evolution during a non-proportional 'shear to tension' load path change using a cross shaped sample. Finite element calculations using an anisotropic plasticity criterion were performed to provide strain and stress state fields. Conclusions on multiple scales are drawn in the following.

On the macroscale:

- A cross shaped sample geometry for 'shear to tension' loading path changes was designed.
- A macro-strain metric was defined and measured optically using the DIC displacement measurements of four points during the mechanical loading, especially during non-proportional load paths. The same procedure was applied to the 3D FE simulations.
- For a load path change of type 'shear to tension' the tension stretch to fracture of is reduced by about 20% compared to the proportional tensile load path.

On the mesoscale:

- An accumulated equivalent strain was chosen that was suited for non-proportional load paths. It was applied to both projection DIC (performed on 3D laminography data) and to the FE simulation results, for the strain measurement in the sample mid plane.
- Similar localization shear bands have been found comparing experimental projection DIC and numerical finite element simulations in terms of shape and magnitude.
- Damage was found at the end of the shear period. The damage evolution was quantified in terms of surface void fraction as a function of the measured accumulated equivalent strain over the entire load history.

On the microscale:

- Two main types of damage features were found: intermetallic particle cracks and (most probably grain-related) flat cracks. The latter are more detrimental in this Al alloy 2198 T8R material.
- Surprisingly damage nucleation could be observed (via laminography) already at the end of shear pre-strain during which stress triaxiality was nearly zero.
- The nucleated damage grew and led to final fracture during tensile loading after the shear pre-strain.

Declaration of Competing Interest

The authors declare that they have no known competing financial interests or personal relationships that could have appeared to influence the work reported in this paper.

Acknowledgment

DFG and ANR (Lambda project:ANR17-CE08-0051; DFG project: 391911929/02012170081) are gratefully acknowledged for their financial support. The European Synchrotron Radiation Facility (ESRF) beamline ID19 is thanked for providing beamtime (experiment ma4333). We thank Constellium C-Tec for materials supply.

References

[1] A. Pineau, A. Benzerga, T. Pardoen, Failure of metals I: brittle and ductile fracture, Acta Mater 107 (2016) 424–483.
[2] Y. Bao, T. Wierzbicki, On fracture locus in the equivalent strain and stress triaxiality space, Int. J. Mech. Sci. 46 (1) (2004) 81–98.
[3] J. Papasidero, V. Doquet, D. Mohr, Ductile fracture of aluminum 2024-t351 under proportional and non-proportional multi-axial loading: bao-wierzbicki results revisited, Int J Solids Struct 69–70 (2015) 459–474.
[4] M. Brünig, M. Zistl, S. Gerke, Numerical analysis of experiments on damage and fracture behavior of differently preloaded aluminum alloy specimens, Metals (Basel) 11 (3) (2021).
[5] A.J. Gross, K. Ravi-Chandar, On the deformation and failure of Al 6061-T6 at low triaxiality evaluated through in situ microscopy, Int. J. Fract. 200 (2016) 185–208.
[6] M. Achouri, G. Germain, P. Dal Santo, D. Saidane, Experimental characterization and numerical modeling of micromechanical damage under different stress states, Materials & Design 50 (2013) 207–222.
[7] E. Maire, P.J. Withers, Quantitative X-ray tomography, Int. Mat. Rev. 59 (1) (2014) 1–43.
[8] C. Landron, E. Maire, J. Adrien, H. Suhonen, P. Cloetens, O. Bouaziz, Non-destructive 3-d reconstruction of the martensitic phase in a dual-phase steel using synchrotron holotomography, Scripta Mat. 66 (12) (2012) 1077–1080.
[9] L. Helfen, T. Baumbach, P. Mikulík, D. Kiel, P. Pernot, P. Cloetens, J. Baruchel, High-resolution three-dimensional imaging of flat objects by synchrotron-radiation computed laminography, Appl Phys Lett 86 (7) (2005) 071915.
[10] C.C. Roth, T.F. Morgeneyer, Y. Cheng, L. Helfen, D. Mohr, Ductile damage mechanism under shear-dominated loading: in-situ tomography experiments on dual phase steel and localization analysis, Int. J. Plast. 109 (2018) 169–192.
[11] T. Tancogne-Dejean, C.C. Roth, T.F. Morgeneyer, L. Helfen, D. Mohr, Ductile damage of aa2024-t3 under shear loading: mechanism analysis through in-situ laminography, Acta Mater 205 (2021) 116556.
[12] T.F. Morgeneyer, L. Helfen, H. Mubarak, F. Hild, 3D digital volume correlation of synchrotron radiation laminography images of ductile crack initiation: an initial feasibility study, Exp Mech 53 (2013) 543–556.
[13] T. Morgeneyer, T. Taillandier-Thomas, L. Helfen, T. Baumbach, I. Sinclair, S. Roux, F. Hild, In situ 3D observation of early strain localisation during failure of thin Al alloy (2198) sheet, Acta Mat. 69 (2014) 78–91.
[14] A. Buljac, F. Hild, L. Helfen, T.F. Morgeneyer, On deformation and damage micromechanisms in strong work hardening 2198 T3 aluminium alloy, Acta Mater 149 (2018) 29–45.
[15] T.F. Morgeneyer, M. Khadyko, A. Buljac, L. Helfen, F. Hild, A. Benallal, T. Børvik, O.S. Hopperstad, On crystallographic aspects of heterogeneous plastic flow during ductile tearing: 3D measurements and crystal plasticity simulations for aa7075-t651, Int. J. Plast. 144 (2021) 103028.
[16] N. Fleck, J. Hutchinson, V. Tvergaard, Softening by void nucleation and growth in tension and shear, J Mech Phys Solids 37 (4) (1989) 515–540.
[17] V. Tvergaard, Shear deformation of voids with contact modelled by internal pressure, Int. J. Mech. Sci. 50 (10) (2008) 1459–1465.
[18] V. Tvergaard, Behaviour of voids in a shear field, Int. J. Fract. 158 (1) (2009) 41–49.
[19] K.L. Nielsen, J. Dahl, V. Tvergaard, Collapse and coalescence of spherical voids subject to intense shearing: studied in full 3D, Int. J. Fract. 177 (2) (2012) 97–108.
[20] M.E. Torki, A.A. Benzerga, A mechanism of failure in shear bands, Extreme Mech Lett 23 (2018) 67–71.
[21] K. Nahshon, J. Hutchinson, Modification of the Gurson model for shear failure, Eur. J. Mech. A/Solids 27 (2008) 1–17.
[22] T. Warner, Recently-developed aluminium solutions for aerospace applications, in: Aluminium Alloys 2006 - ICAA10, in: Materials Science Forum, volume 519, Trans Tech Publications Ltd, 2006, pp. 1271–1278.
[23] T.F. Morgeneyer, T. Taillandier-Thomas, L. Helfen, T. Baumbach, I. Sinclair, S. Roux, F. Hild, In situ 3D observation of early strain localization during failure of thin al alloy (2198) sheet, Acta Mater 69 (2014) 78–91.
[24] A. Buljac, T. Taillandier-Thomas, T.F. Morgeneyer, L. Helfen, S. Roux, F. Hild, Slant strained band development during flat to slant crack transition in AA2198 T8 sheet: in situ 3D measurements, Int. J. Fract. 200 (1) (2016) 49–62.
[25] T.L. Jolu, T.F. Morgeneyer, A.F. Gourgues-Lorenzon, Effect of joint line remnant on fatigue lifetime of friction stir welded Al-Cu-Li alloy, Sci. Technol. Weld. Joining 15 (8) (2010) 694–698.
[26] G. Rousselier, T. Morgeneyer, S. Ren, M. Mazière, S. Forest, Interaction of the Portevin–le Chatelier phenomenon with ductile fracture of a thin aluminum ct specimen: experiments and simulations, Int. J. Fract. 206 (1) (2017) 95–122.
[27] J. Chen, Ductile tearing of AA2198 aluminium-lithium sheets for aeronautic application, École Nationale Supérieure des Mines de Paris, 2011 Theses. https://pastel.archives-ouvertes.fr/pastel-00657028/file/Chen_defintif.pdf
[28] C.C. Roth, D. Mohr, Determining the strain to fracture for simple shear for a wide range of sheet metals, Int. J. Mech. Sci. 149 (2018) 224–240.
[29] X. Kong, D. Missoum-Benziane, T.F. Morgeneyer, Plasticity and ductility of anisotropic AA2198 recrystallized in T351 and T851 condition during proportional and non-proportional loading paths: simulations and experiments, submitted to Journal of Theoretical, Computational and Applied Mechanics (2021). URL https://hal.archives-ouvertes.fr/hal-03497233

[30] T. Belytschko, W. Liu, B. Moran, Nonlinear finite elements for continua and structures, John Wiley & Sons, Ltd, 2000.
[31] A. Abedini, C. Butcher, M. Worswick, Experimental fracture characterisation of an anisotropic magnesium alloy sheet in proportional and non-proportional loading conditions, Int J Solids Struct 144–145 (2018) 1–19.
[32] S. Onaka, Equivalent strain in simple shear deformation described by using the hencky strain, Philos Mag Lett 90 (9) (2010) 633–639.
[33] S. Onaka, Comment on "a comparison of the von mises and hencky equivalent strains for use in simple shear experiments", Philos. Mag. 92 (18) (2012) 2264–2271.
[34] C. Butcher, A. Abedini, Shear confusion: identification of the appropriate equivalent strain in simple shear using the logarithmic strain measure, Int. J. Mech. Sci. 134 (2017) 273–283.
[35] T. Weitkamp, P. Tafforeau, E. Boller, P. Cloetens, J.-P. Valade, P. Bernard, F. Peyrin, W. Ludwig, L. Helfen, J. Baruchel, Parallel-beam imaging at the ESRF beamline ID19: current status and plans for the future, in: R. Garrett, I. Gentle, K. Nugent, S. Wilkins (Eds.), AIP Conference Proceedings, volume 1234, 2010, pp. 83–86.
[36] P.-A. Douissard, A. Cecilia, X. Rochet, X. Chapel, T. Martin, T. van de Kamp, L. Helfen, T. Baumbach, L. Luquot, X. Xiao, J. Meinhardt, A. Rack, A versatile indirect detector design for hard X-ray microimaging, J. Instrum. 7 (2012).
[37] A. Myagotin, A. Voropaev, L. Helfen, D. Hänschke, T. Baumbach, Efficient volume reconstruction for parallel-beam computed laminography by filtered backprojection on multi-core clusters, IEEE Trans. Image Process. 22 (12) (2013) 5348–5361.
[38] M. Vogelgesang, T. Farago, T.F. Morgeneyer, L. Helfen, T. dos Santos Rolo, A. Myagotin, T. Baumbach, Real-time image content based beamline control for smart 4D X-ray imaging, J Synchrotron Radiat 23 (2016) 1254–1263.
[39] A. Buljac, L. Helfen, F. Hild, T.F. Morgeneyer, Effect of void arrangement on ductile damage mechanisms in nodular graphite cast iron: in situ 3D measurements, Eng Fract Mech 192 (2018) 242–261.
[40] J. Besson, R. Foerch, Large scale object-oriented finite element code design, Comput Methods Appl Mech Eng 142 (1) (1997) 165–187.
[41] D. Al Akhrass, J. Bruchon, S. Drapier, S. Fayolle, Integrating a logarithmic-strain based hyperelastic formulation into a three-field mixed finite element formulation to deal with incompressibility in finite-strain elastoplasticity, Finite Elem. Anal. Des. 86 (2014) 61–70.
[42] R. Taylor, A mixed-enhanced formulation for tetrahedral finite elements, Int J Numer Methods Eng 47 (2000) 205–227.
[43] J. Lemaitre, J.-L. Chaboche, Mechanics of Solid Materials, Cambridge University Press, 1990, doi:10.1017/CBO9781139167970.
[44] F. Bron, J. Besson, A yield function for anisotropic materials application to aluminum alloys, Int. J. Plast. 20 (4) (2004) 937–963.
[45] M. Hurst, L. Helfen, H. Suhonen, T.F. Morgeneyer, A. Buljac, J.-P. Suuronen, D. Hänschke, T. Baumbach, Hierarchical 4D imaging by X-ray phase-contrast nano-laminography, submitted (2021).
[46] G. Rousselier, M. Luo, A fully coupled void damage and Mohr-Coulomb based ductile fracture model in the framework of a reduced texture methodology, Int. J. Plast. 55 (2014) 1–24.